

Article

Raspberry Colloid Templated Catalysts Fabricated Using Spray Drying Method

Gabrielle Busto¹, Roza Wineh¹, Hedyeh Zamani¹, Elijah Shirman¹, Sissi Liu¹, Anna V. Shneidman^{1,2} and Tanya Shirman^{1,2,*}

¹ Metalmark Innovations Inc., Cambridge, MA 02138, USA

² Harvard John A. Paulson School of Engineering and Applied Sciences, Cambridge, MA 02138, USA

* Correspondence: tanya@metalmark.xyz or t.shirman@seas.harvard.edu

Abstract: The majority of industrial chemical processes—from production of organic and inorganic compounds to air and water treatment—rely on heterogeneous catalysts. The performance of these catalysts has improved over the past several decades; in parallel, many innovations have been presented in publications, demonstrating increasingly higher efficiency and selectivity. One common challenge to adopting novel materials in real-world applications is the need to develop robust and cost-effective synthetic procedures for their formation at scale. Herein, we focus on the scalable production of a promising new class of materials—raspberry-colloid-templated (RCT) catalysts—that have demonstrated exceptional thermal stability and high catalytic activity. The unique synthetic approach used for the fabrication of RCT catalysts enables great compositional flexibility, making these materials relevant to a wide range of applications. Through a series of studies, we identified stable formulations of RCT materials that can be utilized in the common industrial technique of spray drying. Using this approach, we demonstrate the production of highly porous Pt/Al₂O₃ microparticles with high catalytic activity toward complete oxidation of toluene as a model reaction.

Keywords: heterogeneous catalyst; raspberry colloids; templating; spray drying



Citation: Busto, G.; Wineh, R.; Zamani, H.; Shirman, E.; Liu, S.; Shneidman, A.V.; Shirman, T. Raspberry Colloid Templated Catalysts Fabricated Using Spray Drying Method. *Catalysts* **2023**, *13*, 60. <https://doi.org/10.3390/catal13010060>

Academic Editors: Pedro Tartaj and Narendra Kumar

Received: 26 October 2022

Revised: 21 December 2022

Accepted: 23 December 2022

Published: 28 December 2022



Copyright: © 2022 by the authors. Licensee MDPI, Basel, Switzerland. This article is an open access article distributed under the terms and conditions of the Creative Commons Attribution (CC BY) license (<https://creativecommons.org/licenses/by/4.0/>).

1. Introduction

Chemical production accounts for nearly 25% of energy use worldwide and relies heavily on catalysis, which is used in the synthesis and processing of over 80% of all manufactured products [1–3]. The majority of these processes rely on heterogeneous catalysts, whose phase is distinct from that of reactant mixture (e.g., a solid catalyst in a gaseous or liquid medium). Heterogeneous catalysts are critical in numerous types of chemical synthesis, green technologies, and air pollution abatement, to name a few [4]. However, commercial heterogeneous catalysts employed today tend to exhibit challenges such as migration and sintering of nanoparticles under operational conditions and, consequently, the gradual loss of performance, or alternatively encapsulation of the particles in the support matrix material, rendering them stable but difficult for reactants to access. These drawbacks are typically mitigated by loading the catalyst with an excess quantity of nanoparticles, which are often the most expensive component, for example when produced from Pt group metals (PGMs). The design of a platform technology capable of producing active and stable catalytic systems of varying compositions is essential to improving sustainability, minimizing energy consumption by lowering the required operating temperatures, and improving their environmental impact by reducing waste. An appropriate approach would enable systematic variation and optimization of the individual structural and compositional parameters of the resulting materials, as opposed to sequentially producing one-of-a-kind novel promising compositions, which often entails laborious synthetic procedures [5,6].

Over the last few decades, novel heterogeneous catalysts and synthesis methods have been developed to optimize catalytic performance through the control of their structural

and compositional features [7–9]. For example, the wet chemical hydrothermal method was used to introduce various nano-arrays consisting of 1D nanorods, nanowires or nanotubes directly on 3D monolithic substrates resulting in rationally designed highly efficient catalytic materials [8]. Another novel catalyst group consists of colloid based porous materials (also known as three-dimensional macroporous structure, 3DOM), which possess many advantageous characteristics and degrees of freedom allowing them to be designed for a wide range of catalytic applications including oxidation and reduction of harmful industrial and automotive byproducts, chemical fuels catalysis, biomass upgrading, photocatalysis, and water splitting [9]. Recently, the raspberry colloid templating (RCT) approach was introduced to produce 3DOM catalysts consisting of a fully interconnected porous metal oxide network with metal nanoparticles precisely positioned at the pore/matrix interface, as demonstrated for monometallic Pt, Pd, Ag, Au, and bimetallic Pt/Pd, Ag/Au NPs supported on a variety of metal oxides, including SiO₂, TiO₂, Al₂O₃ [10–13]. The NPs are partially embedded in the metal oxide matrix to provide them with exceptional thermal and chemical stability while partially exposed to the pore interior, which allows their accessibility for reagents. In addition, the resulting macroporosity of these catalytic systems imparted through colloidal templates in the range of 100–400 nm significantly improves material performances arising from the mass transfer enhancement by the macroporous structures, where reactants or adsorbates are quickly transported from the outer surface into the inner pores of the structures. The catalysts have been compared to commercial catalysts and demonstrated improved performance (substantially reduced PGM incorporation and temperatures required) for various reactions (oxidation and hydrogenation tested so far). Yet, another benefit of this method is its modularity which has led to the development of a wide variety of catalyst compositions [14,15].

While promising, few new catalysts, including RCT, have made the leap from the laboratory to industry, most often because scalable synthetic techniques are not yet available for the specific materials. Here, we explore the possibility to apply the standard manufacturing technique of spray drying (SD) to the production of RCT-based microparticles. We have chosen SD as it is a well-known scalable and cost-effective technology used for the bottom-up production of organic, inorganic, and composite powders with controllable size (from nm to μm) and morphology, determined through the choice of process parameters and droplet composition [16,17]. While SD is frequently used in industrial processes including the production of dried foods [18], chemicals, fertilizers, luminescent materials, oxides, ceramics, and pharmaceuticals [19,20], there are a limited number of examples of SD porous catalytic particles prepared using colloid templating [21–23]. One of the possible challenges is the number of components required in a templating method (templating colloid, matrix precursor, and solvent) as the interactions between these components as well as other parameters such as solid content and slurry viscosity will influence the production and final morphology of the SD microparticle.

In this study, we use the RCT approach to synthesize spray dried catalytic microparticles consisting of Pt NPs supported on Al₂O₃ (SD Pt/Al₂O₃). We identified the optimal spray drying conditions and SD slurry formulations to produce uniform, highly porous SD microparticles with Pt NPs uniformly distributed throughout the structure, uniquely at pore/matrix interface, with none fully encapsulated within the matrix. The shape of resulting microparticles is typically toroidal as determined by the multiple components with different sizes and physical properties in spray drying formulation. In contrast, microparticles fabricated from a single component, boehmite nanoparticles (precursor to alumina metal oxide matrix), were typically spherical. We found that loading of Pt NPs on the surface of polymer templating colloids significantly influences the surface morphology of the resulting SD microparticles, attributed to the change in surface charge of the raspberry colloids (polystyrene (PS) spheres decorated with Pt NPs) which in turn destabilizes the interparticle interactions in SD slurry. Our optimized SD process enables the production of hundreds of grams of RCT-based powders per batch with yields of 60–70%. We demonstrate that the SD microparticles have comparable catalytic activity in the oxidation of

toluene (model reaction) to RCT catalysts with the same Pt loading prepared using the initially published lab-scale procedure (Shards Pt/ Al_2O_3) [11,24].

2. Results and Discussion

2.1. Synthesis and Characterization of Raspberry Based SD Micropowders

The general synthetic approach for the fabrication of SD microparticles is shown in Figure 1; synthetic details are provided in the Materials and Methods section below. Briefly, the procedure begins with the synthesis of amidine-capped polystyrene colloids (PS) and Pt NPs; the NPs electrostatically attach to the surface of the PS upon mixing the two suspensions (Step 1). The resulting raspberry colloids simultaneously serve as a template for the resulting porous structure and as vehicles for the precise positioning of metal NPs within the metal oxide matrix. Control over the surface charge of the hybrid particles also determines the interactions with metal oxide precursors in the preparation of SD formulation and is important for the stability of the resulting suspension.

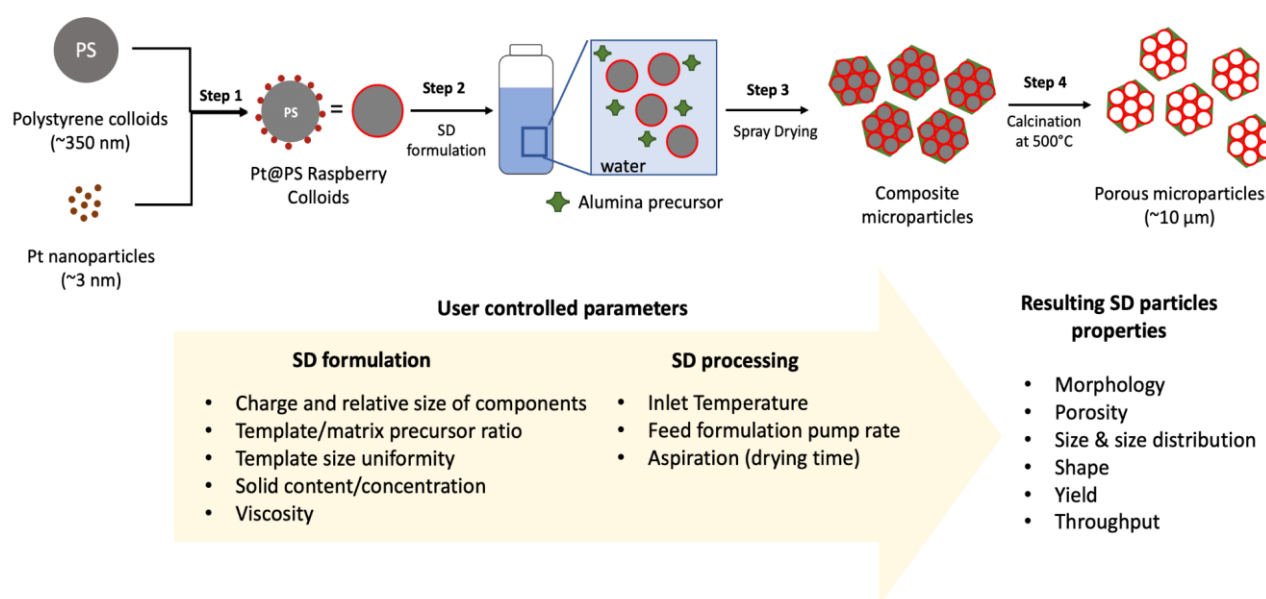


Figure 1. Schematic depicting the process for creating spray-dried (SD) catalytic microparticles using the raspberry colloid templating (RCT) approach.

The SD slurry formulation is formed by combining an aqueous dispersion of the Pt@PS particles formed in Step 1, and a colloidal suspension of boehmite (Bh), the precursor for the supporting alumina matrix (Step 2). Parameters that can be varied in this step are listed at the bottom of Figure 1 and include the mass ratio between the templating colloids and matrix precursors, the relative sizes of each component and their charges, as well as the total concentration of the SD slurry, which determines the slurry viscosity. In this study, both components, raspberry colloids and Bh particles, have a positive charge, resulting in the repulsive interactions that are necessary to stabilize the SD slurry and facilitate the self-assembly process as the droplet dries. Atomization of the slurry (roughly equal-sized droplets generated) in the process of spray drying followed by drying at room temperature (Step 3) results in the formation of composite microparticles, which are then calcined at 500 °C to remove the PS templating colloids; this results in the formation of macroporous Pt/ Al_2O_3 microparticles (Step 4). Our spray drier (Buchi B290) is equipped with a pneumatic multi-fluid nozzle atomizer that can produce droplets in the range of 2–25 μm . As shown at the bottom of Figure 1, spray drying conditions such as temperature, flow rate, and droplet size (mainly defined by the spray dryer type) also significantly affect the SD microparticle structure and morphology. In this study, we kept the spray drying conditions similar for all sample preparation and rather focused on the slurry optimization.

The spray drying parameters were chosen based on our previous studies and included inlet temperature of 160 °C and spray air flow rate of 400 L/h.

When optimizing the procedure, we sought parameters that would result in high quality microparticles exhibiting open surface morphology, which ensures high accessibility of the NPs to reactants, controllable pore size and loading of Pt NPs, as well as the capability to be produced at high yield and large quantity. We tested 3 main parameters that we believed would significantly affect the desired properties: (1) the Pt loading and resulting Pt@PS charge, (2) templating PS size, and (3) SD slurry concentration and resulting viscosity. In this study, we used three different loading of Pt NPs on PS colloids: 0.4Pt@PS, 0.8Pt@PS and 1.6Pt@PS which correspond to 0.4, 0.8 and 1.6 wt.% Pt in the resulting catalytic SD powder, respectively, as determined by inductively coupled plasma mass spectrometry (ICP-MS) measurements. Both the PS colloids and Pt NPs retained their size after they were combined, as determined from SEM and TEM measurements (Figure 2).

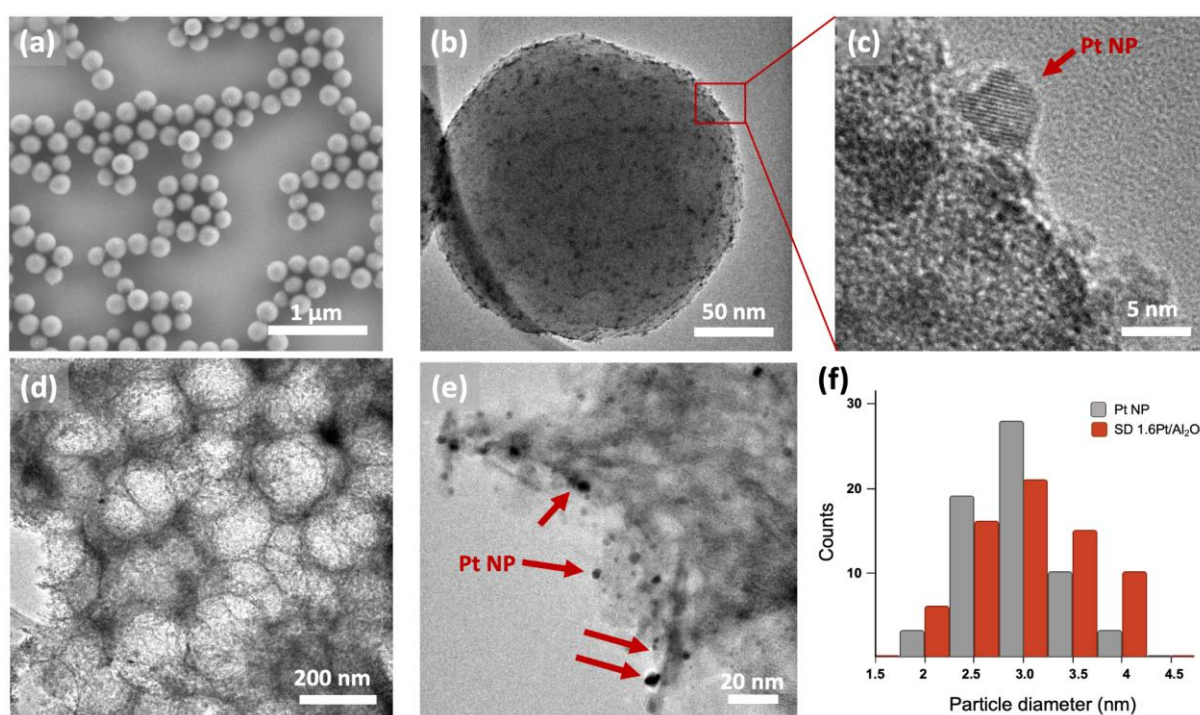


Figure 2. Representative scanning and transmission electron microscopy (SEM and TEM) images of material building blocks and resulting SD 1.6Pt/Al₂O₃ powders synthesized using 1.6Pt@PS raspberry colloids. (a) SEM and TEM (b,c) images of 1.6Pt@PS raspberry colloidal particles with (c) showing a high magnification TEM image of (b) in which the Pt NPs attached to the surface of PS colloid are more clearly visible. (d,e) Representative TEM images of SD 1.6Pt/Al₂O₃ catalyst powders with (e) showing a higher resolution image where Pt NPs are visible at the pore-matrix interface. (f) Histogram of the measured NP size distribution for as-prepared Pt NPs (gray) and those within the RCT SD Pt/Al₂O₃ powder catalyst after calcination at 500 °C (red), values determined from TEM images using ImageJ. At least 100 NP were analyzed. The diameter of NPs before and after calcination were measured to be 2.8 ± 0.5 nm and 3.2 ± 0.7 nm, respectively, indicating only minor sintering.

Studying the effect of Pt loading and templating particle size on microparticle quality. The surface charge and size of the colloidal particles were determined through zeta potential analysis using a Horiba Nanoparticle Analyzer SZ-100 and Scanning Electron Microscopy (SEM), respectively; the results are summarized in Table 1. The amidine capped PS colloids had a positive charge of +46.3 mV and a very narrow size distribution of $\leq 5\%$. The Pt nanoparticles of $2.8 (\pm 0.5)$ nm diameter, were capped with polyvinylpyrrolidone (PVP),

which is negatively charged above its isoelectric point around pH = 3. While this negative charge is necessary for the electrostatic attraction between the nanoparticles and the positively charged amidine groups on the PS surfaces, it also reduces the overall surface charge on the Pt@PS colloids in a Pt-loading-dependent manner.

Table 1. Characterization of the building blocks used to synthesize SD microparticles.

Colloidal Particle	Size and Size Distribution (nm)	Charge (mV)
PS colloids	203.7 (± 11.2)	+46.3
Pt Nanoparticles	2.8 (± 0.5)	−4.5
Boehmite (Bh)	60 (± 17)	30
0.4Pt@PS	203.7 (± 11.2)	+42.5
0.8Pt@PS	203.7 (± 11.2)	+36.7
1.6Pt@PS	203.7 (± 11.2)	+21.5

The Pt loading thus affects the stability of the slurry which also includes positively charged Bh particles, whose measured charge was +30 mV. The size of the Bh particles, measured to be in the range of 60 to 80 nm, is also important as they must fill the interstices of the templating colloids. The Bh nanoparticles were converted to a matrix supporting the NPs and consisted of the desired γ -Al₂O₃ phase after calcination at 500 °C [11]. From our initial studies, the optimal mass ratio of PS to Bh was determined to be in the range of 1.0–1.25. Deviation from this optimum resulted in undesirable structuration of the SD microparticles, with excess Bh in the slurry resulting in compromised porosity or formation of shells, while an insufficient amount resulted in the formation of microparticles with an overall reduced size and incomplete pores [16].

Figure 3 shows SEM images of SD microparticles fabricated using unmodified amidine-capped PS and the same PS decorated with three different amounts of Pt NPs (0.4, 0.8, and 1.6 wt.%). To determine the effects of Pt NPs loading independently of other SD parameters, the SD slurries were kept at 10 wt.% solids, providing similar dynamic viscosities of ~2cP (measured at 60 RPM) and the same spray drying parameters described in the Materials and Methods section. The majority of SD microparticles had an average size in the range of 5–10 microns with a large size distribution, with the final microparticle size and size distribution largely depending on spray drier parameters and process conditions such as nozzle size, inlet temperature, and flow rate [25].

As can be seen from high magnification images in Figure 3 (bottom row) and Figure 4, the average surface pore diameter (D_{sp}) and the number of pores per surface area (surface porosity factor, f_p) strongly depend on the charge of the templating colloids. For an open surface morphology, both the templating particles and the matrix precursor must have a similar surface charge. In our system, the templating colloids and Bh particles were positively charged, though the modification of PS colloids with Pt NPs resulted in a decrease of their positive charge which has an effect on SD particle morphology, as mentioned above. For SD Al₂O₃ and SD 0.4Pt/Al₂O₃ the D_{sp} values were somewhat similar, 146.7 (± 9.8) nm and 160.6 (± 13.7) nm, respectively (Figure 4, gray columns), likely due to the similarity in the charge of the respective templating colloids: 46.3 mV for unmodified amidine capped PS and 42.5 mV for 0.4Pt@PS. Further increase in the Pt loading significantly reduced the charge of the raspberry templating colloids and, consequently, the surface pore diameter in resulting SD microparticles: $D_{sp} = 116.2$ and 65.7 nm for the particles with 0.8 and 1.6 wt.% Pt, respectively (Figure 4, gray columns). In addition to surface pore diameter, the number of pores per surface area had an even larger dependence on templating colloid charge as the reduction of positive charge leads to more Bh particles packing between the templating colloids and thus a larger pore spacing. Determination of the surface porosity factor, f_p , (pore area/total area) was performed by selecting a rectangular area of 1 square micron and measuring the number of pores within that area. The total area of the pores was then calculated by approximating the pores as circles and the porosity factor is calculated as the total area of the pores divided by the area of the rectangle. For SD Al₂O₃ and SD

0.4Pt/Al₂O₃ the f_p values were 0.43 and 0.64, respectively, while for SD microparticles with increased Pt loading of 0.8 and 1.6 wt.% Pt, the f_p values were 0.14 and 0.03, respectively (Figure 4, orange line).

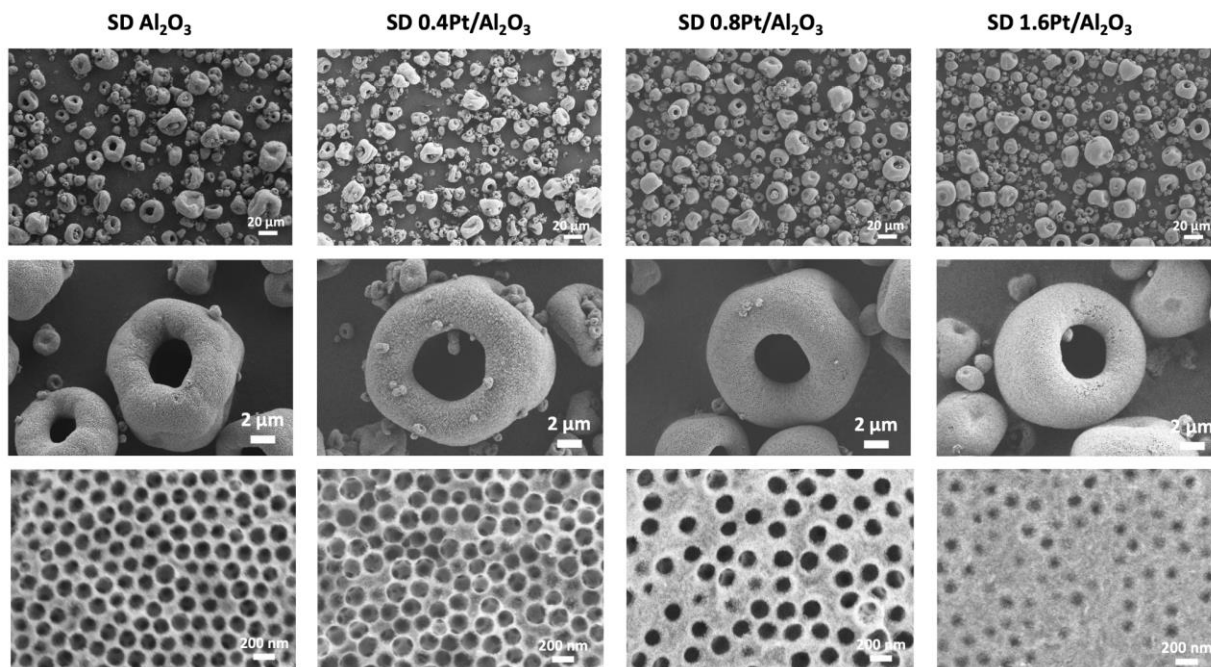


Figure 3. Representative SEM images of porous SD microparticles synthesized using Pt@PS colloids with different loadings of Pt. The weight percent of Pt increases from left to right (0% for the left column, up to 1.6 wt.% for the right one, as determined through post-synthesis ICP-MS analysis, and indicated in the column header). The magnification of the SEM images increases from top to bottom. Samples were prepared using 200 nm PS particles and a slurry concentration of 10 wt.%.

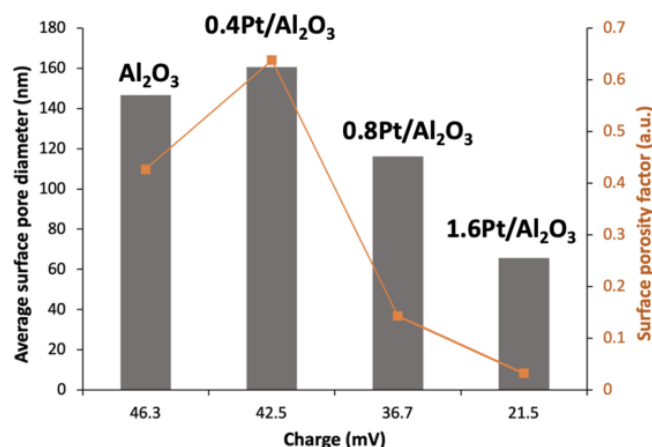


Figure 4. Average surface pore diameter (gray columns) and surface porosity factor (orange line) for different loadings of Pt (which correspond to a different templating colloid charge). Size and morphology of the SD powders were analyzed using ImageJ image processing software. At least 80 microparticles were analyzed.

The decrease in surface porosity can also be seen in Figure 3: a partial shell consisting of aluminum oxide appears on the surface of SD. This is likely due to the de-mixing of the particles during droplet drying due to differences in surface charge, wherein the smaller, more positively charged particles are first transported to the meniscus region and form a thin shell at the air/droplet interface. These results together identified that the surface

charge threshold for effective electrostatic repulsion between colloids and boehmite to yield open surface morphology is around 30 mV. Interestingly, the reduction in pore diameter and partial shell formation was observed only on the surface of SD microparticles, while the internal porosity was open as desired even for SD 1.6Pt/Al₂O₃ (Figure 2d–e). For all SD microparticles, the internal pore diameter was measured to be ~180 nm which is smaller than that of the templating PS spheres by ~10% due to the shrinkage of the Al₂O₃ that occurs during thermally induced template removal. The average diameter of Al₂O₃-supported Pt NPs was 3.2 ± 0.7 nm, which is very similar to that of the initially synthesized Pt NPs (2.8 ± 0.5 nm, Figure 2f and Table 1).

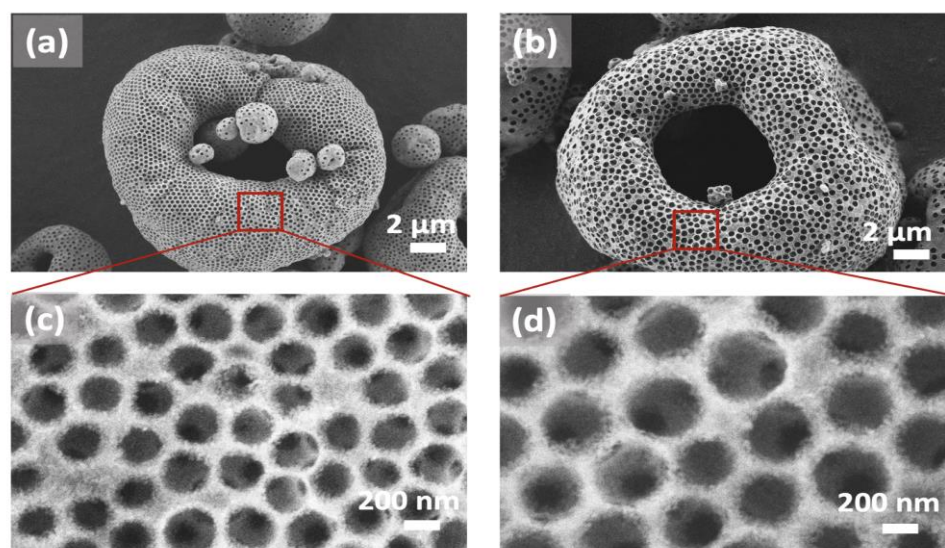
Finally, the SD microparticles of larger sizes (~10 μm) demonstrate buckled, toroidal shapes. The deviation from spherical shape was readily observed in other studies, especially in multicomponent systems [16,20,26,27], wherein various parameters such as process conditions (e.g., temperature, injection rate) and physicochemical properties of the colloidal suspensions can introduce instabilities and distort the stable spherical shape to produce a plethora of shapes including buckled spheres, deflated balloons, donuts, etc. While the majority of studies on the physical origin of these instabilities or buckling focus on SD slurries with single type of colloidal particles [26], much less is known about buckling effects in multicomponent systems demonstrating complex interplay between different physicochemical parameters of each component [27,28], especially when one of the components is also a composite material (like the raspberry particles used here). The problem is complex by nature as it entails the hydrodynamics of jets and the drying of colloidal suspensions, during which colloidal interactions tend to play a crucial role.

During the drying process, solvent evaporation from the droplet induces a capillary flow to the gas–liquid interface and emerging interparticle capillary forces self-assemble the particles into closely packed arrangements at the droplet–air interface where they form a “colloidal shell”. The final shape of the microparticles depends on the structural stability and permeability of this shell: stable, denser shells with less permeability for hot air will buckle to form donut-like structures, while a dynamic, liquid-like shell with high permeability will promote the further isotropic shrinkage of the droplet upon drying and produce spherical particles [26]. Interestingly, the fabrication of SD microparticles using the same spray drying parameters without templating colloids resulted in the fabrication of spherical particles instead of donuts (Figure A1). The resulting spheres have similar size and size distribution which is not affected by solid content of the slurry (Figure A1b,c). In addition, for templated microparticles, the size of the droplet plays an important role in the final shape of the particles. As can be seen from Figure 3 top and bottom images and Figure A2, most of the microparticles with ≤ 2 μm size have spherical shape or very minimal deformation from the sphere. These results were observed in many other publications in which most microparticles with micron and sub-micron size fabricated using co-assembly of templating colloids and metal oxide precursors resulted in spherical microparticles [21,29–31].

A combination of optical characterization and focused ion beam (FIB) together with SEM have been used previously to reveal the internal structure of 3D colloidal assemblies, produced by drying drops fabricated via emulsification microfluidics [32], a lab-scale technique that produces orders of magnitude fewer particles (milligram scale) than the SD presented here. Optical microscopy of those so-called “photonic balls” showed a strong photonic reflection peak, while FIB and SEM followed by image processing revealed a layered morphology of the colloidal crystal with a polycrystalline, close-packed lattice at the interface and disordered core. In contrast, the pore arrangement in the SD particles looks qualitatively non-crystalline (Figure 3, bottom row). This can be explained by the relative rates of assembly in the SD vs. photonic ball approaches. In general, for 3D assembly within a drying droplet, the crystallization process is frustrated in the curved confinement, which introduces disorder and defects into the final microparticles. The extent of disorder depends to a large degree on the relative sizes of the droplet and templating colloids as well as the mobility of the colloids within the droplet. Unlike the gradual drying of particles produced by microfluidics, SD drives the assembly process at a fast

pace, resulting in kinetically trapped disordered assemblies. Nevertheless, we were able to achieve interconnectivity of the porous structures (e.g., SD 0.4Pt/Al₂O₃) with catalytic nanoparticles embedded within the walls yet exposed to the interior of the pores and greatly accessible by reactants (Figure 2e)—qualities that are critical for enhancing activity and stability of heterogeneous catalysts.

Control over the porosity of SD microparticles. The pore size of RCT-based materials is determined by the size of the templating colloids. Implementation of materials exhibiting interconnected mesoporous networks such as RCT materials can enhance both internal mass and heat transfer, and active site dispersion and accessibility, particularly valuable for applications such as liquid phase catalysis and biomass conversion. Figure 5a,b show images of SD 0.4Pt/Al₂O₃ synthesized using PS colloids with diameters of 385 nm and 420 nm, respectively. Increasing the size of PS colloids results in slightly increased surface charge but still yields highly porous SD microparticles with open surface morphology and high surface porosity factor (Figure 5e).



(e)	PS diameter (nm)	Charge of template (mV)	Surface pore diameter, D_{sp} (nm)	Surface Porosity factor, f_p
SD PS-200	203.7 (\pm 11.2)	42.5	160.6 (\pm 13.7)	0.64
SD PS-380	385.6 (\pm 7.8)	43.1	330.2 (\pm 17.3)	0.60
SD PS-490	420.0 (\pm 18.8)	48.5	410.7 (\pm 20.2)	0.61

Figure 5. Control over pore diameter in SD microparticles using various sizes of PS templating colloids. (a,b) SEM images of RCT SD 0.4Pt@PS with PS sizes of 385.6 nm (a,c) and 420.0 nm (b,d), respectively. (e) Table summarizing the measured results.

Studying the effects of SD slurry concentration on yield, throughput, and microparticle qualities. For the SD process to be cost effective, the throughput needs to be maximized without compromising the morphology and structure of the SD microparticles and process yield. Many parameters, both for spray drying conditions (aspiration, inlet temperature, pump rate) and SD formulation (concentration, viscosity), can affect the yield and throughput of SD microparticles production; however, they can simultaneously perturb the quality of the particle microstructure, i.e., their porosity. One of the ways to increase the production of material is to increase the concentration of precursors in SD slurry formulations. Figure 6a,b shows SEM images of SD 0.4Pt/Al₂O₃ microparticles synthesized from slurry formulations with 15 wt.% and 20 wt.% solid content, respectively. Figure 6c shows the analysis (ImageJ software) of SD particle size for all three concentrations, used in this

experiment. Based on this analysis, we did not observe a significant increase in SD particle size with an increase in slurry concentration, with the majority of the particles in the range of 6–10 microns. Importantly, no effect on the particle's morphology was observed, with all samples demonstrating high surface porosity (insets on Figure 6a,b).

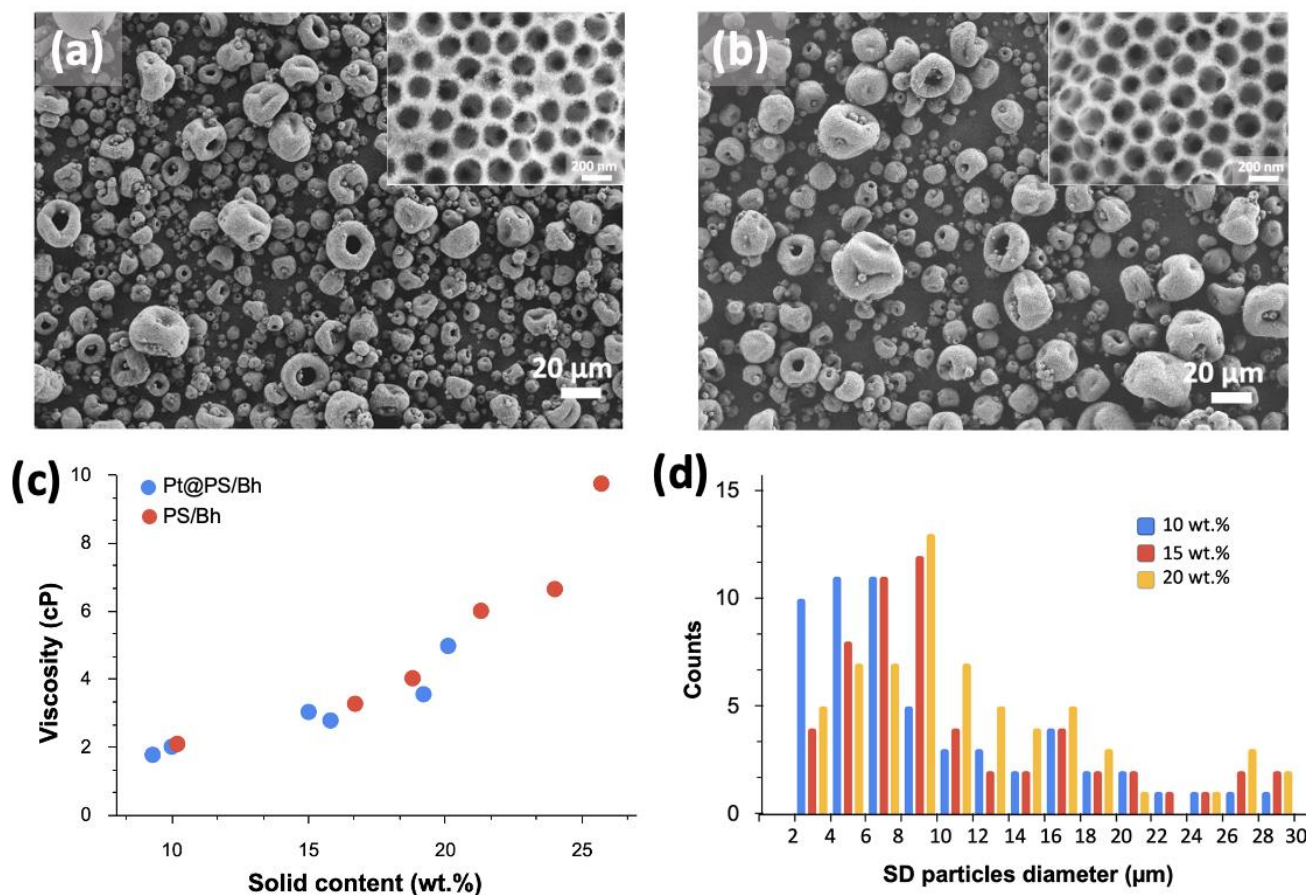


Figure 6. Effect of initial slurry concentration on the viscosity of the SD slurry and resulting SD particles size. (a,b) SEM images of SD 0.4Pt/Al₂O₃ microparticles synthesized using 0.4Pt@PS slurry formulation with 15 wt.% and 20 wt.%, respectively. (c) Viscosity of slurries made from different concentrations of precursors. Red dots correspond to slurries formed from unmodified PS (not Pt) with boehmite nanoparticles, while blue dots correspond to 0.4Pt@PS and boehmite formulations. All slurry viscosities were measured at 60 RPM. (d) Size and size distribution of SD particles created using different initial slurry concentrations.

Further increasing the slurry concentration was not possible due to the spray drier properties such as the nozzle dimensions that limits the range of usable viscosities (upper limit of 10cP for the B290 spray dryer we use here, according to manufacturer specifications). As can be seen in Figure 6c, the increase in solid content increases the viscosity of the formulation leading to the maximum range of solids of 20–25 wt.%. Using high solid content slurries with optimized SD synthetic parameters allowed the fabrication of hundreds of grams of RCT-based SD micropowders and the yield remained 60–70% for all concentrations.

2.2. Evaluation of Catalytic Activity of SD Microparticles

In order to evaluate the functionality of the resulting SD microparticles, we tested them in a flow reactor towards the oxidation of toluene (model reaction) and compared them to RCT Pt/Al₂O₃ synthesized using a previously published lab-scale evaporative co-assembly method known as “Shards” [11,24]. For the two types of particles: SD microparticles and

Shards, we studied both 0.4Pt@PS and 1.6Pt@PS. Figure 7a,b show SEM images of Shards RCT 1.6Pt/Al₂O₃ catalytic powder (here, as before, the number before Pt denotes the final wt.% of the platinum in the catalytic powder determined by ICP-MS). The catalytic powder synthesized via spray drying using Pt@PS colloids had essentially the same structure as Shards counterparts. Shards RCT 1.6Pt/Al₂O₃ consisted of randomly shaped particles in the range of 10–200 μm with interconnected ~190 nm diameter spherical voids; unlike SD particles of the same Pt wt.%, there had an open surface morphology, confirming that the process conditions affect this aspect. The size of the macropores was smaller than that of the templating PS spheres by ~11% due to the shrinkage of the alumina framework that occurs during thermally induced template removal, exactly as for the SD microparticles [11]. The average diameter of Al₂O₃-supported Pt NPs was measured to be 3.8 ± 0.7 nm (TEM images in Figure 7c), which was very similar to that of the initially synthesized Pt NPs (2.8 ± 0.5, Table 1).

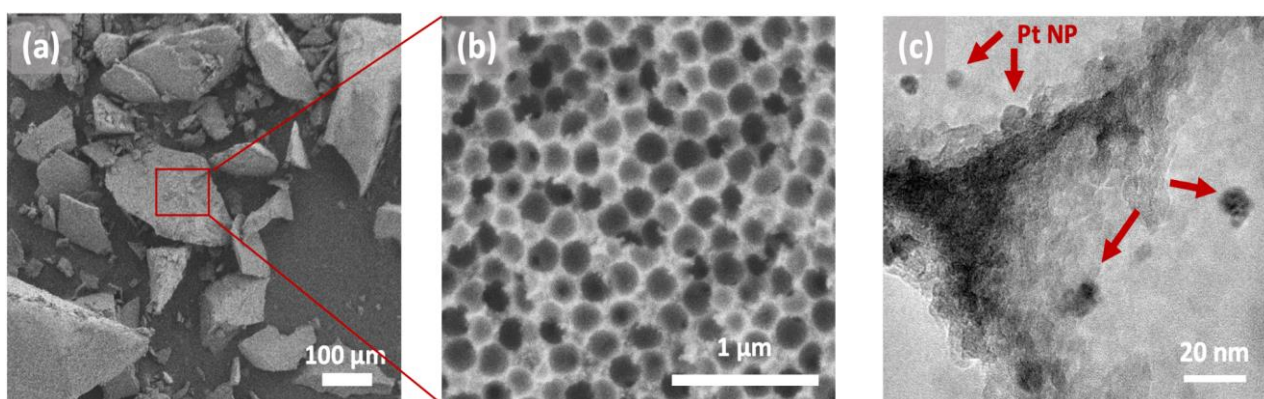


Figure 7. Representative scanning and transmission electron microscopy (SEM and TEM) images of Pt/Al₂O₃ powders synthesized using a conventional method (Shards) and building blocks shown in Figure 2. (a,b) SEM images of Pt/Al₂O₃ powder particles with the interconnected porous network visible in the high magnification image (b); (c) high resolution TEM image of Pt NPs (dark dots) supported on alumina.

X-ray photoelectron spectroscopy (XPS) measurements were carried out to determine the valence states of metal Pt NPs supported on RCT alumina as the oxidation state of supported Pt NPs has been found to play an important role in the catalytic activity toward oxidation of VOCs [33,34]. Figure A3a shows the results of the survey XPS spectra of a shards RCT 1.6Pt/Al₂O₃ catalyst sample. As the Al 2p and Pt 4f lines overlap, making the XPS signal difficult to analyze, the Pt 4d_{5/2} signal was analyzed instead [35]. As can be seen from Figure A3b, the binding energies (BE) of Pt/Al₂O₃ sample are in the range of 315.0–315.7 eV, characteristic of oxidized Pt species and agree with the values reported in the literature (reported values for PtO and PtO₂ are 315.3 eV and 317 eV, respectively [35]). The oxidized Pt species on the surface of Pt NPs results from the calcination step in air at 500 °C for 2 h during the preparation of the porous particles. When the Pt NP supported on alumina are reduced via, for example, heat treatment under reducing atmosphere of H₂, the BE was reported to be around 314.6 eV which corresponds to metallic Pt [35]. The effect of the reducing atmosphere on catalytic performance of RCT Pt/Al₂O₃ systems can be examined in a future study.

The typical reactant feed was 10 ppm of toluene in dry air. The total flow rate of the feed gas was kept constant at 0.5 L/min; for both SD and Shards, the total mass of material was kept at ~100 mg. The results of the study are shown in Figure 8a,b. No intermediates or byproducts were detected during the oxidation reaction. Table 2 summarizes the light-off temperatures for the studied catalysts. The catalytic activities were evaluated by measured values of T₁₀ and T₉₀, defined as the temperatures corresponding to 10% and 90% toluene conversion, respectively. Figure 8a reveals that the catalytic activity of SD 0.4Pt/Al₂O₃

catalysts is very similar to that of its Shards counterparts, with slightly lower T_{90} of 120 °C compared to the Shards 0.4Pt/Al₂O₃ catalysts (T_{90} = 128 °C). Increasing the Pt loading from 0.4 wt.% to 1.6 wt.% decreased the toluene oxidation temperature for Shards 1.6Pt/Al₂O₃ from T_{90} = 128 °C to T_{90} = 115 °C (Figure 8b, Table 2). As can be seen from Figure 7b the surface of Shards has open porosity.

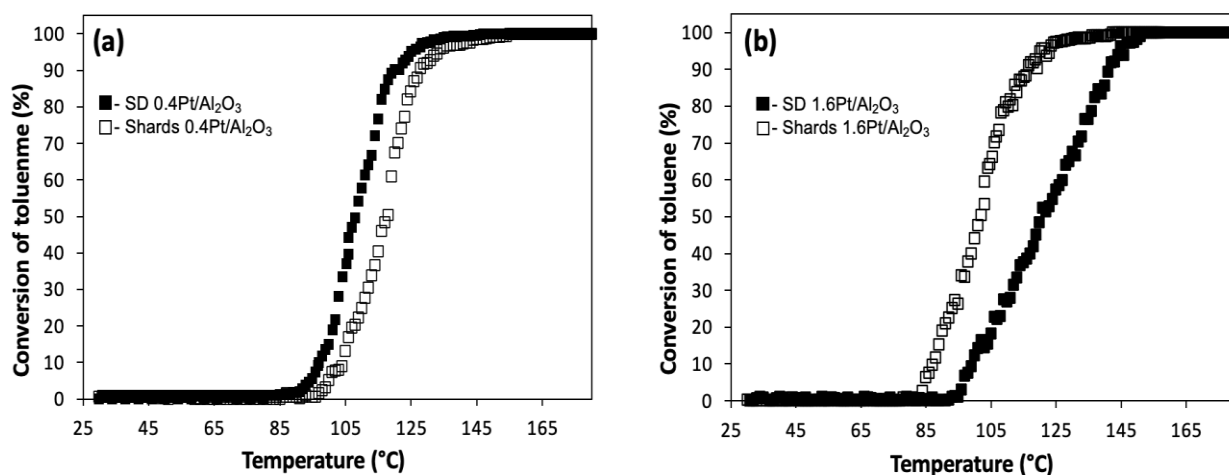


Figure 8. Light-off curves of conversion of toluene to CO₂ as a function of reaction temperature for RCT samples of SD microparticles and Shards with different Pt loadings: (a) 0.4 wt.% Pt, and (b) 1.6 wt.% Pt. Reaction conditions: catalyst mass 100 mg, 10 ppm toluene in dry air, flow rate of 0.5 L/min, and gas hourly space velocity (GHSV) ~ 5000 h⁻¹.

Table 2. Comparison of temperatures required for 10% (T_{10}) and 90% (T_{90}) conversions of toluene for the SD microparticles and Shards with different Pt loadings.

Catalyst	T_{10} (°C)	T_{90} (°C)
SD 0.4Pt/Al ₂ O ₃	97	120
Shards 0.4Pt/Al ₂ O ₃	104	128
SD 1.6Pt/Al ₂ O ₃	100	142
Shards 1.6Pt/Al ₂ O ₃	87	115

In contrast, SD 1.6Pt/Al₂O₃ microparticles showed reduction in catalytic activity as T_{90} was increased from 120 °C to 142 °C, which is likely due to the mostly closed surface morphology of this catalyst that was described in the previous section (Figure 3). Taken together, these results show that the surface morphology of the catalyst plays an important role in its catalytic activity.

As mentioned previously, the modularity of raspberry templated approach in the synthesis of catalyst allows control over multiple parameters simultaneously. For example, the control over metal nanoparticles size and size distribution. As was demonstrated previously, the exceptional thermal stability of various metal nanoparticles incorporated via raspberry approach can allow the study of NP size effect on catalytic performance [10,11,14]. Such control is important for establishing structure-property relationships for many types of catalytic material [36,37]. The composition of the matrix material can be also easily controlled to expand the choice of support, including mixed metal oxides to study the effect of metal-support interactions and effect of support acidic sites [38]. The modularity of RCT approach allows the design of advantageous catalyst and capability of scaling up using SD method, as demonstrated in this paper, opens the future utilization of this advanced catalyst in real world applications”.

3. Materials and Methods

3.1. Chemical Reagents

Styrene ($\geq 99\%$, stabilized with 4-tertbutylcatechol), 2,2'-azobis(2-methylpropionamide) dihydrochloride (AAH) (97–98%), chloroplatinic acid hexahydrate ($\text{H}_2\text{PtCl}_6 \cdot 6\text{H}_2\text{O}$, $\geq 37.5\%$ Pt by weight), sodium borohydride (NaBH_4 , 98%), and polyvinylpyrrolidone (PVP, MW 10,000 Da) were purchased from Sigma Aldrich (St. Louis, MO, USA). All chemicals were used as received. Deionized (DI) water was used for all experiments.

3.2. Synthesis of SD Powders

3.2.1. Synthesis of Building Blocks

The amidine capped PS colloids, Pt NPs, and Pt@PS raspberry colloids were synthesized using published procedures [11,24].

3.2.2. Preparation of Slurry for SD

The SD slurry formulation was prepared by mixing Pt@PS colloidal solution with aqueous dispersion of Bh (mass ratio PS/Bh = 1) and stirred magnetically for 10 min to form desired final concentration of SD slurry.

3.2.3. Synthesis of Catalytic SD Powders

The above prepared slurry was spray dried using a Buchi B290 mini spray dryer with two fluid nozzles having an inner diameter of 0.7 mm. The temperature at the inlet was kept at 160 °C and the air flow rate at 400 L/h for all experiments. Following spray drying, the resulting powder was calcined at 500 °C for 4 h at a heating rate of 10 °C/min to remove the templating PS colloids and convert boehmite to γ -alumina.

3.3. Characterization

The solid contents of the solutions and slurries were measured with a moisture analyzer (Mettler Toledo, HG63 Halogen Moisture Analyzer, Columbus, OH, USA). The size and charge of precursors (PS, Pt NP and Pt@PS) were measured by dynamic light scattering (DLS) and zeta potential analysis was performed with a Horiba Nanoparticle Analyzer SZ-100 (Horiba, Kyoto, Japan). Six scans were performed for each DLS measurement and 3 scans for each zeta potential measurement. Slurry viscosity was measured with a Brookfield viscometer with spindle 00 and the small sample adapter. Transmission electron microscopy (TEM) images were acquired using a JEOL 2100 microscope (Japan) with an operating voltage of 200 kV. The samples for TEM images were made by placing a drop of the NP solution or a finely ground powder of solid sample on a TEM carbon-coated grid. High-resolution images were taken using a Gatan Osiris digital camera (Pleasanton, CA, USA). The size distribution of metal NPs was measured using ImageJ image processing software (LOCI, University of Wisconsin). At least 100 individual NPs were counted and analyzed. Scanning Electron Microscopy (SEM) images were acquired using an FESEM Ultra55 (Zeiss, Germany). Size and morphology of the SD powders were analyzed using ImageJ image processing software. At least 80 individual SD particles were counted and analyzed. X-ray photoelectron spectroscopy (XPS) measurements were performed using Thermo Scientific K-Alpha (Waltham, MA, USA) with 180° double focusing hemispherical analyzer with 128-channel detector. A k-alpha microfocused monochromator was used as the X-ray source.

3.4. Catalytic Tests

The catalytic activity of the powders was evaluated using a custom fixed bed microreactor at atmospheric pressure. Samples of ~100 mg of fine catalytic powder were mixed with ~500 mg of quartz sand, and the mixture was loaded into a fritted quartz tube, sandwiched by glass wool. The fritted quartz tube was custom-made with 1/2 diameter and an embedded quartz frit in the middle (Finkenbeiner.com). The micro-reactor was located in the isothermal zone of an electric furnace. The temperature of the furnace was set using

a PID controller (The Mellen Company Inc., Concord, NH, USA). A K-type thermocouple immersed in the catalytic bed was used to control and monitor the temperature of the bed during the run. All of the lines before and after the reactor were heated to 130 °C to prevent condensation. Prior to the experiments, the powder catalyst was dried under a dry air flow at 150 °C for 30 min. Afterwards, the bed was cooled down to ~30 °C. All experiments were started by flowing dry air in the microreactor to acquire the baseline concentration. Each experiment was carried out at a gas hourly space velocity (GHSV) of ~5000 h⁻¹ and a total flow rate of 0.5 L/min. For each experiment, a 200 ppm toluene gas cylinder was diluted by dry air to ~10 ppm using mass flow controllers and was fed through the microreactor. Then, the powder catalyst was gradually heated to the desired temperature by 1 °C/min. Light-off curves were obtained by monitoring the concentration of the components in the exhaust stream using a Multigas 2030 FTIR gas analyzer (MKS Instruments, Inc., Wilmington, MA, USA). The FTIR was equipped with a liquid-nitrogen cooled mercury-cadmium-telluride detector and a silicon carbide infrared light source. Baseline measurements for the FTIR were performed daily using 0.5 L/min dry air. Spectra were recorded every six seconds with a 0.5 cm⁻¹ resolution. MG2000 software was used to record the spectra and analyze the gas composition.

4. Conclusions

Here, we described the scalable synthesis of porous spray-dried raspberry-colloid templated (RCT) microparticles using spray drying. We deduced that the loading of catalytic nanoparticles on the templating colloidal particles determines the microporosity of the resulting SD particles, as a greater quantity of NPs reduces the positive surface charge on the colloids, while that of the matrix precursor remains at a higher positive value. Of the different loadings tested, we determined that 0.4 wt.% Pt generated the most open surface porosity, which is critical to catalytic activity, as we demonstrated when comparing SD 0.4Pt/Al₂O₃ and SD 1.6Pt/Al₂O₃ microparticles. The ones with 0.4 wt.% loading showed much higher activity towards the model reaction of toluene oxidation than 1.6Pt/Al₂O₃ microparticles due to the closed surface pores for the higher weight percent SD particles, despite 4 times higher loading of catalytic nanoparticles. Since increasing the NP loading reduces the microparticle quality, further research can be conducted to optimize the synthetic parameters and the Pt@PS charge, for example through adjustment of the slurry pH or by changing the capping ligand, in order to achieve higher Pt incorporation without disrupting the beneficial microstructure of the SD particles.

We also determined that, within the range of tested conditions (10–20% solid content), the concentration of the slurry does not have a significant effect on the size and surface morphology of SD microparticles, as long as the charge of templating colloids is within the right range. Likewise, the microparticle size and size distribution, yield, and morphology remain similar, at least within this range of slurry concentrations.

The shape of the catalytic particles was toroidal, though this is another aspect that can be explored further as the requirements can differ according to application. For example, for pharmaceutical applications, the morphology requirements may differ according to the route of administration of the powder (e.g., oral vs. inhalation). For catalytic application, the donut shape may be beneficial over dense spherical particles as it has larger surface area and better mass and heat transfer properties. Other parameters which were kept constant in these studies can also be varied in order to increase the yield, Pt loading, and other important aspects: monodispersity of colloids, PS/Bh ratio, SD flow rate, inlet temperature, etc. By translating these studies to industrial-scale spray dryers, it should be possible to scale up this process even further to make RCTs relevant to a variety of real-world applications.

Author Contributions: Conceptualization E.S. and T.S.; methodology, supervision, and writing T.S.; data analysis T.S., G.B., H.Z. and R.W.; synthesis, characterization and validation T.S., G.B., H.Z. and R.W.; data curation, T.S.; writing—review and editing, T.S., E.S., S.L. and A.V.S. All authors have read and agreed to the published version of the manuscript.

Funding: This research was funded by the NSF SBIR Phase II Grant Number 2026128.

Acknowledgments: This work was performed in part at the Harvard University Center for Nanoscale Systems (CNS), a member of the National Nanotechnology Coordinated Infrastructure Network (NNCI), which is supported by the National Science Foundation under NSF ECCS award no. 1541959. We thank Oleg Ilinich for helpful discussions.

Conflicts of Interest: The authors declare no conflict of interest.

Appendix A

Factors affecting SD microparticles morphology: effect of templating colloids and size of the droplets.

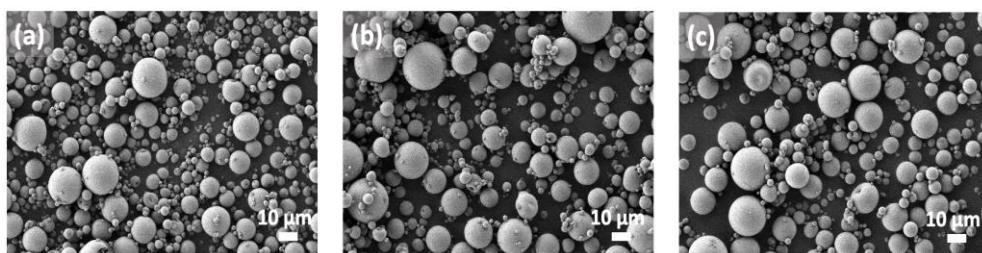


Figure A1. SEM images of SD microparticles synthesized without templating colloids using Bh as Al_2O_3 precursor and the same spray drying parameters. (a) 10 wt.% SD slurry; (b) 15 wt.% SD slurry; (c) 20 wt.% SD slurry.

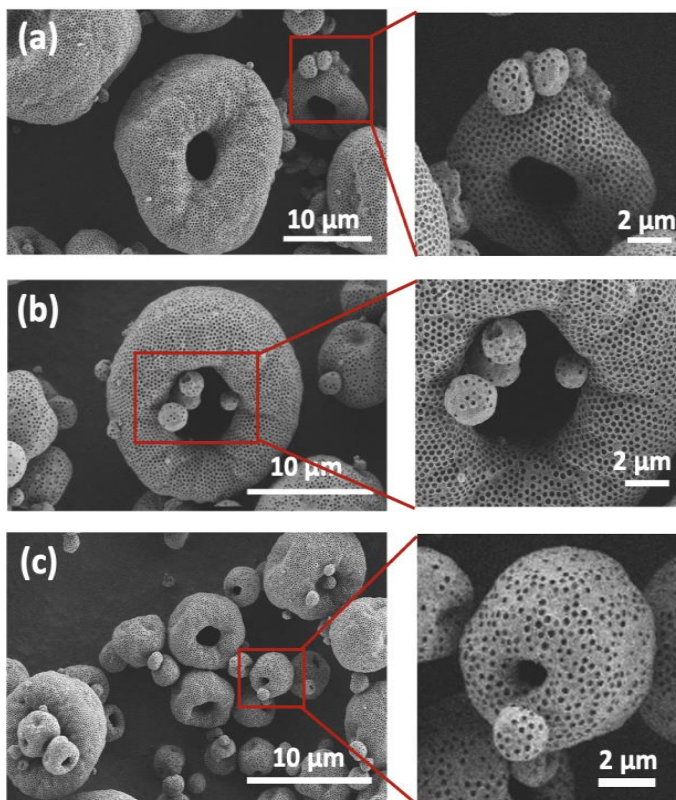


Figure A2. SEM images of SD microparticles synthesized using 0.4Pt@PS with PS sizes of 385.6 nm at different SD slurry concentrations. (a) 10 wt.%; (b) 15 wt.%; (c) 20 wt.%. Microparticles with $\leq 2 \mu\text{m}$ diameter have spherical shape as demonstrated on zoomed in images on the right.

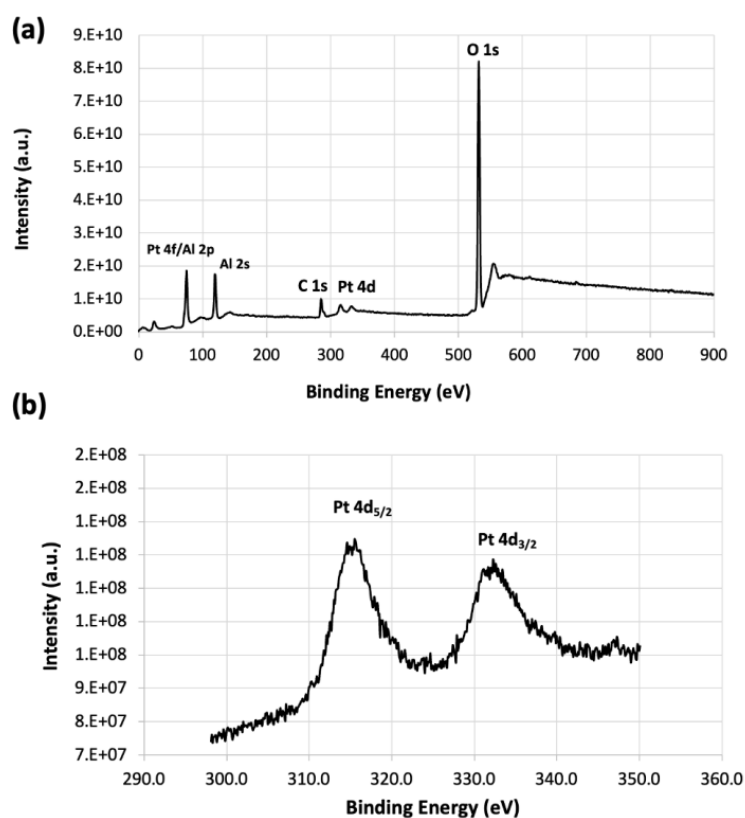


Figure A3. XPS spectra of RCT 1.6Pt/Al₂O₃ powder: (a) survey XPS and (b) Pt 4d XPS spectra.

References

1. Catlow, R.; Davidson, M.; Hardacre, C.; Hutchings, G.J. Catalysis makes the world a better place. *Phil. Trans. R. Soc. A* **2016**, *374*, 20150089. [CrossRef]
2. Available online: <http://cdn.exxonmobil.com/mediaglobal/files/outlook-forenergy-outlook-for-energy.pdf> (accessed on 1 September 2022).
3. Worrell, D.E.; Phylipsen, D.; Einstein, N.M. *Energy Use and Energy Intensity of the U.S. Chemical Industry*; Energy Analysis Department, Ernest Orlando Lawrence Berkeley National Laboratory, University of California: Berkeley, CA, USA, 2000.
4. Hagens, J. Heterogeneously Catalyzed Processes in Industry. In *Book Industrial Catalysis: A Practical Approach*, 3rd ed.; Wiley VCH Verlag GmbH & Co. KGaA: Weinheim, Germany, 2015; pp. 261–298.
5. Hansen, T.; Delariva, A.; Challa, S.R.; Datye, A.K. Sintering of catalytic nanoparticles: Particle migration or Ostwald ripening? *Acc. Chem. Res.* **2013**, *46*, 1720–1730. [CrossRef]
6. Campbell, C.T. The energetics of supported metal nanoparticles: Relationships to sintering rates and catalytic activity. *Acc. Chem. Res.* **2013**, *46*, 1712–1719. [CrossRef]
7. Munnik, P.; de Jongh, P.E.; de Jong, K.P. Recent developments in the synthesis of supported catalysts. *Chem. Rev.* **2015**, *115*, 6687–6718. [CrossRef]
8. Wang, S.; Ren, Z.; Guo, Y.; Gao, P.-X. Nano-array integrated monolithic devices: Toward rational materials design and multi-functional performance by scalable nanostructures assembly. *CrystEngComm* **2016**, *18*, 2980–2993. [CrossRef]
9. Parlett, C.M.A.; Karen Wilson, K.; Lee, A.F. Hierarchical porous materials: Catalytic applications. *Chem. Soc. Rev.* **2013**, *42*, 3876–3893. [CrossRef]
10. Shirman, E.; Shirman, T.; Shneidman, A.V.; Grinthal, A.; Phillips, K.R.; Whelan, H.; Bulger, E.; Abramovitch, M.; Patil, J.; Nevarez, R.; et al. Modular design of advanced catalytic materials using hybrid organic–inorganic raspberry particles. *Adv. Funct. Mater.* **2018**, *28*, 1704559. [CrossRef]
11. Shirman, T.; Toops, T.J.; Shirman, E.; Shneidman, A.V.; Liu, S.; Gurkin, K.; Alvarenga, J.; Lewandowski, M.P.; Aizenberg, M.; Aizenberg, J. Raspberry colloid-templated approach for the synthesis of palladium-based oxidation catalysts with enhanced hydrothermal stability and low temperature activity. *Catal. Today* **2021**, *360*, 241. [CrossRef]
12. Luneau, M.; Guan, E.; Chen, W.; Foucher, A.C.; Marcella, N.; Shirman, T.; Verbart, D.M.A.; Aizenberg, J.; Aizenberg, M.; Stach, E.A.; et al. Enhancing catalytic performance of dilute metal alloy nanomaterials. *Commun. Chem.* **2020**, *3*, 46–51. [CrossRef]
13. van der Hoeven, J.E.S.; Krämer, S.; Dussi, S.; Shirman, T.; Park, K.-C.K.; Rycroft, C.H.; Bell, D.C.; Friend, C.M.; Aizenberg, J. On the origin of sinter-resistance and catalyst accessibility in raspberry-colloid-templated catalyst design. *Adv. Funct. Mater.* **2021**, *31*, 2106876. [CrossRef]

14. van der Hoeven, J.E.S.; Shneidman, A.V.; Nicolas, N.J.; Aizenberg, J. Evaporation-induced self-assembly of metal oxide inverse opals: From synthesis to applications. *Acc. Chem. Res.* **2022**, *55*, 1809–1820. [[CrossRef](#)] [[PubMed](#)]
15. Han, J.H.; Shneidman, A.V.; Kim, D.Y.; Nicolas, N.J.; van der Hoeven, J.E.S.; Aizenberg, M.; Aizenberg, J. Highly ordered inverse opal structures synthesized from shape-controlled nanocrystal building blocks. *Angew. Chem. Int. Ed.* **2021**, *61*, e202111048.
16. Stunda-Zujeva, A.; Irbe, Z.; Berzina-Cimdina, L. Controlling the morphology of ceramic and composite powders obtained via spray drying—A review. *Ceram. Int.* **2017**, *43*, 11543–11551. [[CrossRef](#)]
17. Nandiyanto, A.B.D.; Okuyama, K. Progress in developing spray-drying methods for the production of controlled morphology particles: From the nanometer to submicrometer size ranges. *Adv. Powder Technol.* **2011**, *22*, 1–19. [[CrossRef](#)]
18. Gharsallaoui, A.; Roudaut, G.; Chambin, O.; Voilley, A.; Saurel, R. Applications of spray-drying in microencapsulation of food ingredients: An overview. *Food Res. Int.* **2007**, *40*, 1107–1121. [[CrossRef](#)]
19. Debecker, D.P.; Le Bras, S.; Boissiere, C.; Chaumonnot, A.; Sanchez, C. Aerosol processing: A wind of innovation in the field of advanced heterogeneous catalysts. *Chem. Soc. Rev.* **2018**, *47*, 4112–4155. [[CrossRef](#)]
20. Vehring, R. Pharmaceutical particle engineering via spray drying. *Pharm. Res.* **2008**, *25*, 999–1022. [[CrossRef](#)]
21. Nandiyanto, A.B.D.; Ogi, T.; Wang, W.-N.; Gradon, L.; Okuyama, K. Template-assisted spray-drying method for the fabrication of porous particles with tunable structures. *Adv. Powder Technol.* **2019**, *30*, 2908–2924. [[CrossRef](#)]
22. Iskandar, F.; Nandiyanto, A.B.D.; Yun, K.M.; Hogan, C.J.; Okuyama, K.; Biswas, P. Enhanced photocatalytic performance of brookite TiO₂ macroporous particles prepared by spray drying with colloidal templating. *Adv. Mater.* **2007**, *19*, 1408–1412. [[CrossRef](#)]
23. Cho, Y.-S. Fabrication of hollow or macroporous silica particles by spray drying of colloidal dispersion. *J. Dispers. Sci. Technol.* **2016**, *37*, 23–33. [[CrossRef](#)]
24. Shirman, T.; Shirman, E.; Shneidman, A.V.; Lattimer, J.; Htet, Y.; Gurkin, K.B.; Liu, S.; Aizenberg, M.; Aizenberg, J. Advanced nanostructured catalysts for efficient in-cabin air purification. In Proceedings of the 49th International Conference on Environmental Systems ICES-2019-157, Boston, MA, USA, 7–11 July 2019.
25. Liu, W.; Chenc, X.D.; Selomulya, C. On the spray drying of uniform functional microparticles. *Particuology* **2015**, *22*, 1–12. [[CrossRef](#)]
26. Parikh, D.M. *Handbook of Pharmaceutical Granulation Technology*; Informa Healthcare: New York, NY, USA, 2005.
27. Lintingre, E.; Lequeux, F.; Talini, L.; Tsapisc, N. Control of particle morphology in the spray drying of colloidal suspensions. *Soft Matter* **2016**, *12*, 7435–7444. [[CrossRef](#)] [[PubMed](#)]
28. Sen, D.; Melo, J.S.; Bahadur, J.; Mazumder, S.; Bhattacharya, S.; Ghosh, G.; Dutta, D.; D'Souza, S.F. Buckling-driven morphological transformation of droplets of a mixed colloidal suspension during evaporation-induced self-assembly by spray drying. *Eur. Phys. J. E* **2010**, *31*, 393–402. [[CrossRef](#)] [[PubMed](#)]
29. Abdullah, M.; Iskandar, F.; Shibamoto, S.; Ogi, T.; Okuyama, K. Preparation of oxide particles with ordered macropores by colloidal templating and spray pyrolysis. *Acta Mater.* **2004**, *52*, 5151–5156. [[CrossRef](#)]
30. Nandiyanto, A.B.D.; Hagura, N.; Iskandar, F.; Okuyama, K. Design of a highly ordered and uniform porous structure with multi sized pores in film and particle forms using a template-driven self-assembly technique. *Acta Mater.* **2010**, *58*, 282–289. [[CrossRef](#)]
31. Le, P.H.; Kitamoto, Y.; Le, K.; Cao, A.; Hirano, T.; Tanabe, E.; Ogi, T. Synthesis of macroporous three-way catalysts via template-assisted spray process for enhancing mass transfer in gas adsorption. *Adv. Powder Technol.* **2022**, *33*, 103581. [[CrossRef](#)]
32. Vogel, N.; Utech, S.; England, G.T.; Shirman, T.; Phillips, K.R.; Koay, N.; Burgess, I.B.; Kolle, M.; Weitz, D.A.; Aizenberg, J. Color from hierarchy: Diverse optical properties of micron-sized spherical colloidal assemblies. *Proc. Natl. Acad. Sci. USA* **2015**, *112*, 10845–10850. [[CrossRef](#)]
33. Gana, T.; Chub, X.; Qic, H.; Zhanga, W.; Zoua, Y.; Yana, W.; Liu, G. Pt/Al₂O₃ with ultralow Pt-loading catalyze toluene oxidation: Promotional synergistic effect of Pt nanoparticles and Al₂O₃ support. *Appl. Catal. B* **2019**, *257*, 117943. [[CrossRef](#)]
34. Huang, H.; Leung, D.Y.C.; Ye, D. Effect of reduction treatment on structural properties of TiO₂ supported Pt nanoparticles and their catalytic activity for formaldehyde oxidation. *J. Mater. Chem.* **2011**, *21*, 9647–9652. [[CrossRef](#)]
35. Riguette, B.A.; Damyanova, S.; Gouliev, G.; Marques, C.M.P.; LacPetrou, L.; Bueno, J.M.C. Surface behavior of Alumina-supported Pt catalysts modified with cerium as revealed by X-ray Diffraction, X-ray Photoelectron Spectroscopy, and Fourier Transform Infrared Spectroscopy of CO adsorption. *J. Phys. Chem. B* **2004**, *108*, 5349–5358. [[CrossRef](#)]
36. Radic, N.; Grbic, B.; Terlecki-Baricevic, A. Kinetics of deep oxidation of n-hexane and toluene over Pt/Al₂O₃ catalysts: Platinum crystallite size effect. *Appl. Catal. B* **2004**, *50*, 153–159. [[CrossRef](#)]
37. Sanchez, S.I.; Menard, L.D.; Bram, A.; Kang, J.H.; Small, M.W.; Nuzzo, R.G.; Frenkel, A.I. The Emergence of non-bulk properties in supported metal clusters: Negative thermal expansion and atomic disorder in Pt nanoclusters supported on γ -Al₂O₃. *J. Am. Chem. Soc.* **2009**, *131*, 7040–7054. [[CrossRef](#)] [[PubMed](#)]
38. Jiang, Z.; Chen, D.; Deng, W.; Guo, L. Different morphological ZSM-5 zeolites supported Pt catalysts for toluene catalytic combustion. *Chem. Phys. Impact* **2022**, *5*, 100134. [[CrossRef](#)]

Disclaimer/Publisher's Note: The statements, opinions and data contained in all publications are solely those of the individual author(s) and contributor(s) and not of MDPI and/or the editor(s). MDPI and/or the editor(s) disclaim responsibility for any injury to people or property resulting from any ideas, methods, instructions or products referred to in the content.